Finite element modelling of perturbed stellar systems

Mir Abbas Jalali*

Sharif University of Technology, Postal Code: 14588-89694, Azadi Avenue, Tehran, Iran

3 November 2018

ABSTRACT

I formulate a general finite element method (FEM) for self-gravitating stellar systems. I split the configuration space to finite elements, and express the potential and density functions over each element in terms of their nodal values and suitable interpolating functions. General expressions are then introduced for the Hamiltonian and phase space distribution functions of the stars that visit a given element. Using the weighted residual form of Poisson's equation, I derive the Galerkin projection of the perturbed collisionless Boltzmann equation, and assemble the global evolutionary equations of nodal distribution functions. The FEM is highly adaptable to all kinds of potential and density profiles, and it can deal with density clumps and initially non-axisymmetric systems. I use ring elements of non-uniform widths, choose linear and quadratic interpolation functions in the radial direction, and apply the FEM to the stability analysis of the cutout Mestel disc. I also integrate the forced evolutionary equations and investigate the disturbances of a stable stellar disc due to the gravitational field of a distant satellite galaxy. The performance of the FEM and its prospects are discussed.

Key words: celestial mechanics, stellar dynamics – galaxies: kinematics and dynamics – galaxies: spiral – galaxies: interactions – methods: analytical – methods: numerical

INTRODUCTION

Schwarzschild's (1979) orbit superposition method, N-body simulations (Binney & Tremaine 2008) and smoothed particle hydrodynamics (SPH) (Springel & Hernquist 2002; Springel 2005) have been the main simulation tools of dynamical processes in star clusters, galaxies and dark matter halos. As parallel computers are developed and specialpurpose hardware cards emerge (Sugimoto et al. 1990; Makino et al. 2003; Portegies Zwart, Belleman & Geldof 2007: Portegies Zwart et al. 2008: Gaburov, Harfst & Portegies Zwart 2009), the resolution of simulations is enhanced too. Nevertheless, the number of particles that the most sophisticated codes and hardwares can handle, still lags realistic figures by several orders of magnitude. Combined with the problem of setting initial conditions for a given galaxy, this technological limitation leaves the ground open for alternative methods like a direct search for the solutions of the Boltzmann equation. One such an idea was introduced in Jalali (2007), where the variational weighted residual form of the collisionless Boltzmann equation (CBE) was used to study the modal structure of disc galaxies, and the CBE was projected onto a system of ordinary differential equations.

The success of variational methods, however, depends

* mjalali@sharif.edu (MAJ)

on the potential-density basis sets used in the derivation of test and trial functions. For instance, after 15 to 20 terms, inappropriate test and trial functions may contribute more to the noise than building the perturbed density in clumpy regions or in cusps. Our choices of potential-density basis functions are indeed limited both for discs (Clutton-Brock 1972; Kalnajs 1976; Qian 1992, 1993) and for three dimensional systems (Clutton-Brock 1973; Hernquist & Ostriker 1992; Zhao 1996; Rahmati & Jalali 2009), and it is not always possible to systematically find/tailor (Saha 1991; Robijn & Earn 1996; Weinberg 1999) suitable potentialdensity pairs for a given galaxy model. We thus need a unified methodology with adaptively controlled resolution, and capable of modeling arbitrary density profiles.

The existence of different kinds of orbits in a stellar system further complicates the governing dynamics. It is a routine procedure to work with initially axisymmetric disc galaxies because their phase space is filled by rosette orbits. In natural systems, however, small asymmetries generate higher-order resonant orbits, the angular momentum of individual orbits is no longer conserved and finding a physical phase space distribution function (DF) demands accurate knowledge about resonant tori. In such conditions, N-body and SPH simulations may lead to unrealistic results, especially near sharp clumps (Agertz et al. 2007) or at the boundaries of resonant tori: the stars of thin tori may be totally missed in simulations or they 2

may cause noise and artificial heating rather than participating in local/global structure formation. Schwarzschild's (1979) method can still be trusted when it comes to taking into account (theoretically) all possible orbit families, but it cannot be efficiently applied to the modeling of transient processes. In this study, I present a finite element method (FEM) for investigating the time-dependent evolution of stellar systems. Over half a century, the FEM has undoubtedly played a crucial role in structural engineering, geophysics and fluid dynamics (Zienkiewicz, Taylor & Zhu 2005; Lewis, Nithiarasu & Seetharamu 2004; Parker et al. 2008), but its application to stellar dynamics is initiated here.

After a brief review of orbit calculations on resonant tori, I formulate a finite element technique in the configuration space for solving Poisson's equation/integral, and describe the perturbed potential and density functions of a disc galaxy in the vicinity of a general non-axisymmetric equilibrium. I then express the distribution and Hamiltonian functions in terms of local angle-action variables on tori and over finite elements. I derive a relation between nodal densities and DFs, and use Galerkin's projection to obtain a system of ordinary differential equations for the temporal evolution of DF. I discuss the nature of evolutionary equations in the absence and presence of external perturbers, and validate my FEM code by investigating the linear stability problem of the stellar Mestel disc. I then study the disturbances induced by a satellite galaxy on its primary stellar disc. I conclude the paper by comparing the FEM with other techniques, and discuss about its possible developments.

2 FINITE ELEMENT FORMULATION

The evolution of a stellar system near a given equilibrium state is described by the phase space DF

$$f(\mathbf{x}, \mathbf{v}, t) = f_0(\mathbf{x}, \mathbf{v}) + f_1(\mathbf{x}, \mathbf{v}, t), \tag{1}$$

where $\boldsymbol{x}=(x,y,z)$ and $\boldsymbol{v}=(v_x,v_y,v_z)$ are, respectively, the Cartesian coordinates (of stars) and their conjugate momenta, and t is the time. The subscripts 0 and 1 denote equilibrium and perturbed states, respectively. In a collisionless system the function f is conserved along the orbits of stars and one has

$$\frac{\partial f}{\partial t} + [f, \mathcal{H}] = 0, \tag{2}$$

where $[\cdots, \cdots]$ is the Poisson bracket taken over the (x, v)-space, and

$$\mathcal{H}(\mathbf{x}, \mathbf{v}, t) = \frac{1}{2} \mathbf{v} \cdot \mathbf{v} + \Phi_0(\mathbf{x}) + \Phi_1(\mathbf{x}, t) + \Phi_e(\mathbf{x}, t), \tag{3}$$

is the Hamiltonian function that governs the motion of stars subject to the mean-field potential $\Phi_0(\boldsymbol{x}) + \Phi_1(\boldsymbol{x},t)$ due to self-gravity, and a weak external field $\Phi_e(\boldsymbol{x},t)$. The equilibrium and perturbed self-gravitational potentials are related to the densities $\rho_j = \int f_j \mathrm{d}^3 \boldsymbol{v}$ through Poisson's equation $\nabla^2 \Phi_j = 4\pi G \rho_j \ (j=0,1)$ where G is the universal constant of gravitation. For discs, this equation is replaced by Poisson's integral

$$\Phi_j = -G \int \frac{\Sigma_j d^2 x'}{|x' - x|},\tag{4}$$

where $\Sigma_j = \int f_j d^2 v$ is the surface density. I am interested in solving the CBE for time-varying systems, so the perturbed potential and density functions depend on t, explicitly.

Regular orbits of the initial Hamiltonian system

$$\mathcal{H}_0(\mathbf{x}, \mathbf{v}) = \frac{1}{2} \mathbf{v} \cdot \mathbf{v} + \Phi_0(\mathbf{x}), \tag{5}$$

lie on invariant tori, and the set of tori with common central periodic orbits constitute a resonant bundle. I focus on initially integrable systems whose resonant bundles are separated by the invariant manifolds of unstable periodic orbits. Non-integrability is usually associated with the destruction of invariant manifolds and the occurrence of a layer of chaotic orbits. Resonant bundles associated with \mathcal{H}_0 can be constructed in terms of the action variables J and their conjugate angles w (McGill & Binney 1990; Kaasalainen & Binney 1994a,b), and the phase space coordinates of stars are determined from

$$\mathbf{x}(t) = \sum_{k} \mathbf{X}_{k}(\mathbf{J})e^{\mathrm{i}\mathbf{k}\cdot\mathbf{w}}, \quad \mathbf{w} = \mathbf{\Omega}t + \mathbf{w}_{0}, \quad \mathrm{i} = \sqrt{-1},$$
 (6)

$$\mathbf{v}(t) = \sum_{k} i(\mathbf{k} \cdot \mathbf{\Omega}) \mathbf{X}_{k}(\mathbf{J}) e^{i\mathbf{k} \cdot \mathbf{w}}. \quad \mathbf{X}_{k}^{*}(\mathbf{J}) = \mathbf{X}_{-k}(\mathbf{J}).$$
 (7)

Here k is a vector of integer numbers, $\Omega = \partial \mathcal{H}_0/\partial J$ is the vector of orbital frequencies and asterisk stands for complex conjugation. Substituting from (6) and (7) into f(x, v, t) and $\mathcal{H}(x, v, t)$ leads to

$$f = f_0(\mathbf{J}) + f_1(\mathbf{w}, \mathbf{J}, t), \quad f_1 = \operatorname{Re} \sum_{\mathbf{k}} \tilde{f}_{1,\mathbf{k}}(\mathbf{J}, t) e^{i\mathbf{k}\cdot\mathbf{w}}, \quad (8)$$

$$\mathcal{H} = \mathcal{H}_0(\mathbf{J}) + \Phi_1(\mathbf{w}, \mathbf{J}, t) + \Phi_e(\mathbf{w}, \mathbf{J}, t), \tag{9}$$

so that

$$\Phi_1 = \operatorname{Re} \sum_{k} \tilde{h}_{1,k}(\boldsymbol{J}, t) e^{i\boldsymbol{k} \cdot \boldsymbol{w}}, \qquad (10)$$

$$\Phi_{\rm e} = \operatorname{Re} \sum_{\mathbf{L}} \tilde{h}_{{\rm e},\mathbf{k}}(\mathbf{J},t) e^{\mathrm{i}\mathbf{k}\cdot\mathbf{w}}. \tag{11}$$

The dependency of f_0 only on the action variables is deduced from Jeans theorem. I intend to determine the functions $\tilde{f}_{1,k}(J,t)$ and $\tilde{h}_{1,k}(J,t)$ over a set of finite elements. The advantage of using angle-action variables is that physical quantities are modelled in terms of Fourier series over half of the phase space. I continue with the finite element formulation of stellar discs and the generalisation of the same procedure to three dimensional systems will be presented elsewhere.

2.1 Finite ring elements in the configuration space

Adopting the usual polar coordinates (R, ϕ) , where R is the radial distance from the galactic centre and ϕ is the azimuthal angle, the 2π -periodicity of physical quantities in the ϕ -direction suggests the Fourier expansions of the perturbed potential and surface density as

$$\Phi_1(R,\phi,t) = \operatorname{Re} \sum_{m=-\infty}^{+\infty} P_m(R,t) e^{\mathrm{i}m\phi}, \qquad (12)$$

$$\Sigma_1(R,\phi,t) = \operatorname{Re} \sum_{m=-\infty}^{+\infty} S_m(R,t) e^{\mathrm{i}m\phi}.$$
 (13)

The configuration space is then split to N ring elements. The width of the nth element is obtained using its nodal radii R_n and R_{n+1} as $\Delta R_n = R_{n+1} - R_n$, and the functions $P_m(R,t)$ and $S_m(R,t)$ are approximated by

$$P_m(R,t) = \sum_{n=1}^{N} H_n(R) \mathbf{G}_n \cdot \mathbf{a}_m^n, \qquad (14)$$

$$S_m(R,t) = \sum_{n=1}^{N} H_n(R) \mathbf{G}_n \cdot \mathbf{b}_m^n, \tag{15}$$

$$H_n(R) = \begin{cases} 1, & R_n \le R \le R_{n+1}, \\ 0, & R < R_n \text{ or } R > R_{n+1}. \end{cases}$$
 (16)

The elements of the $N_{\rm d}$ -dimensional row vector

$$G_n = \begin{bmatrix} G_{1n}(R) & G_{2n}(R) & \cdots & G_{N_{\mathbf{d}}n}(R) \end{bmatrix}, \tag{17}$$

are suitable interpolating functions (also known as shape functions) in the R-domain, and the N_d -dimensional column vectors \boldsymbol{a}_m^n and \boldsymbol{b}_m^n are time-dependent nodal amplitudes defined by

$$\boldsymbol{a}_{m}^{n} = \begin{bmatrix} a_{1m}^{n}(t) & a_{2m}^{n}(t) & \cdots & a_{N_{d}m}^{n}(t) \end{bmatrix}^{T}, \tag{18}$$

$$\boldsymbol{b}_{m}^{n} = \begin{bmatrix} b_{1m}^{n}(t) & b_{2m}^{n}(t) & \cdots & b_{N_{d}m}^{n}(t) \end{bmatrix}^{\mathrm{T}}.$$
 (19)

Here a superscript T stands for transpose and a dot denotes matrix/vector multiplication. The parameter $N_{\rm d}$ is the number of nodes in a single element, and we have the general property $G_{jn}(\bar{R}_k) = \delta_{jk}$, where δ_{jk} is the Kronecker delta and \bar{R}_k is the radial position of the kth node in the normalised coordinate:

$$\bar{R} = 2\frac{R - R_n}{\Delta R_n} - 1. \tag{20}$$

The simplest one dimensional element is obtained for $N_{\rm d}=2$ by using the linear functions

$$G_{1n} = \frac{1}{2}(1 - \bar{R}), \quad G_{2n} = \frac{1}{2}(1 + \bar{R}).$$
 (21)

For $N_{\rm d} > 2$, higher-order elements with $N_{\rm d} - 2$ interior nodes are built. The interpolating functions of a quadratic element of the so-called serendipity family are

$$G_{1n} = \frac{\bar{R}^2 - \bar{R}}{2}, \ G_{2n} = 1 - \bar{R}^2, \ G_{3n} = \frac{\bar{R} + \bar{R}^2}{2}.$$
 (22)

These linear and quadratic functions are of C_0 class, which guarantee that $S_m(R,t)$ and $P_m(R,t)$ are smooth (continuous and differentiable) inside elements and continuous at the boundary nodes should the amplitude functions satisfy

$$a_{N_{\mathbf{d}}m}^{n} = a_{1m}^{(n+1)}, \quad b_{N_{\mathbf{d}}m}^{n} = b_{1m}^{(n+1)}, \quad n \ge 1.$$
 (23)

On substituting from (12) and (13) into (4) and changing the integration variables to polar coordinates, one obtains

$$P_m(R,t) = \lim_{\epsilon \to 0} \left[\frac{-2G}{\sqrt{R}} \int_0^\infty dR' \sqrt{R'} S_m(R',t) \right] \times Q_{m-1/2} \left(\frac{\epsilon^2 + R^2 + R'^2}{2RR'} \right),$$
 (24)

where $Q_{\nu}(z)$ is the associated Legendre function of the second kind. The parameter ϵ is introduced to handle the divergence of $Q_{\nu}(z)$ at |z|=1. although $Q_{m-1/2}(1)$ is indefinite, the limit of the whole bracketed statement in (24) exists as $\epsilon \to 0$. I substitute the series of (14) and (15) into (24), take the inner product of the resulting equation by $H_{n'}(R) G_{n'}^{\mathrm{T}}$

and carry out the integrations over R and R' to obtain

$$a_m^{n'}(t) = -2G \sum_{n=1}^{N} \left[\mathbf{A}^{-1}(n') \cdot \mathbf{B}(m, n', n) \right] \cdot b_m^n(t),$$
 (25)

for $n'=1,2,\cdots,N$. Equation (25) is the Galerkin projection (or weighted residual form) of Poisson's integral over the n'th element. The constant $N_{\rm d} \times N_{\rm d}$ matrix ${\bf A}$ is defined as

$$\mathbf{A}(n) = \int_{R_n}^{R_{n+1}} \mathbf{G}_n^{\mathrm{T}}(R) \cdot \mathbf{G}_n(R) \, \mathrm{d}R, \tag{26}$$

and the elements of the $N_{\rm d} \times N_{\rm d}$ matrix $\mathbf{B} = [B_{ij}]$ are computed from

$$B_{ij}(m, n', n) = \lim_{\epsilon \to 0} \int_{R_{n'}}^{R_{n'+1}} \int_{R_n}^{R_{n+1}} \sqrt{\frac{R'}{R}} G_{in'}(R) G_{jn}(R')$$

$$\times Q_{m-1/2} \left(\frac{\epsilon^2 + R^2 + R'^2}{2RR'} \right) dR' dR. \quad (27)$$

Considering the conditions in (23), nodal potentials and densities can be collected, respectively, in the column vectors

$$\boldsymbol{p}_m(t) = \begin{bmatrix} p_m^1(t) & p_m^2(t) & \cdots & p_m^{N_t}(t) \end{bmatrix}^{\mathrm{T}}, \tag{28}$$

$$\boldsymbol{d}_{m}(t) = \begin{bmatrix} d_{m}^{1}(t) & d_{m}^{2}(t) & \cdots & d_{m}^{N_{t}}(t) \end{bmatrix}^{T}, \tag{29}$$

with $N_{\rm t}$ being the total number of boundary and interior nodes. The system of $N_{\rm d} \times N$ linear equations (25) is thus assembled to

$$\boldsymbol{p}_m(t) = \mathbf{C}(m) \cdot \boldsymbol{d}_m(t),\tag{30}$$

where $\mathbf{C}(m)$ is a generally dense $N_{\rm t} \times N_{\rm t}$ constant matrix. Equation (30) relates a discrete set of densities to their corresponding potentials.

As an example, I use the FEM and construct the potential functions associated with Clutton-Brock's (1972) density functions

$$\sigma_j^m(R) = \frac{2m+2j+1}{2\pi b^2} \left(\frac{b^2}{R^2+b^2}\right)^{3/2} P_i^m \left(\frac{R^2-b^2}{R^2+b^2}\right), \quad (31)$$

where b is a length scale and P_i^m are associated Legendre functions with i=m+j. The functions σ_j^m are oscillatory versus R when $j\geq 1$. Figure 1a displays $\sigma_2^2(R)$ for b=1. I use linear interpolation functions with $N_{\rm d}=2$, and divide the R-domain to N=25 ring elements whose nodal radii are determined using the rule (there are no interior nodes)

$$R_n = -\alpha_1 \ln \left(1 - \frac{1}{2(N+1)} - \frac{n-1}{N+1} \right). \tag{32}$$

The width ΔR_n of elements increases as one departs from the galactic centre. The parameter α_1 determines the concentration of elements near the centre (or at large radii). Filled circles in Figure 1a mark the nodal densities $\sigma_2^2(R_n)$ $(n=1,2,\cdots,N+1)$ that have been computed from (31) for $\alpha_1=2$. There is no time-dependence for a static mass distribution. The corresponding nodal potentials are therefore computed through solving the linear system (30) for p_m . Figure 1b shows the potential $\psi_2^2(R)$ calculated using Clutton-Brock's exact formula (solid line) and the FEM (scattered triangles). The agreement between analytical and finite element solutions is impressive: while the maximum magnitude

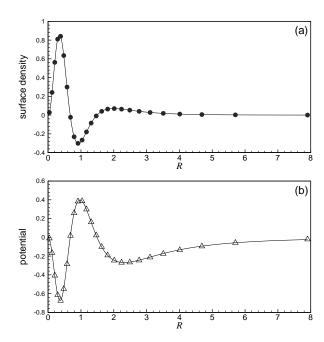


Figure 1. (a) The graph of $\sigma_2^2(R)$ (solid line) and the nodal densities (filled circles) used in equation (30). (b) Exact analytical potential $\psi_2^2(R)$ (solid line) associated with $\sigma_2^2(R)$ and the finite element solution p_m (triangles) for N=25.

of $|\psi_2^2(R)|$ is 0.674, the root mean squared error

$$E_{\rm rms} = \left\{ \frac{1}{N+1} \sum_{i=1}^{N+1} \left[p_m^i - \psi_2^2(R_j) \right]^2 \right\}^{1/2}, \tag{33}$$

is $E_{\rm rms}=0.0035$ for N=25 and it drops to $E_{\rm rms}=0.00097$ for N=50. Although the results are improved by further increasing the number of elements, switching to quadratic elements is more effective. I added an interior node to the elements described in (32) and used (22) with $N_{\rm d}=3$ to compute the potential function $\psi_2^2(R)$. For N=50 elements, I found $E_{\rm rms}=0.000296$, which is lower by a factor of ≈ 3.3 than the error corresponding to the same number of linear elements.

2.2 Transformations to the angle-action space

To determine $\tilde{f}_{1,k}(\boldsymbol{J},t)$, I assume

$$\tilde{f}_{1,k}(\boldsymbol{J},t) = \sum_{n=1}^{N} \boldsymbol{E}_{k}(n,\boldsymbol{J}) \cdot \boldsymbol{z}_{k}^{n}(t), \tag{34}$$

where the elements of the $N_{
m d}$ -dimensional row vectors

$$\boldsymbol{E}_{k}(n,\boldsymbol{J}) = \begin{bmatrix} E_{1,k}(n,\boldsymbol{J}) & E_{2,k}(n,\boldsymbol{J}) & \cdots & E_{N_{d},k}(n,\boldsymbol{J}) \end{bmatrix}, (35)$$

are interpolation functions in the J-space and the time-dependent $N_{\rm d}$ -dimensional column vectors

$$\boldsymbol{z}_{k}^{n}(t) = \begin{bmatrix} \boldsymbol{z}_{1,k}^{n}(t) & \boldsymbol{z}_{2,k}^{n}(t) & \cdots & \boldsymbol{z}_{N_{d},k}^{n}(t) \end{bmatrix}^{T},$$
 (36)

are the nodal DFs. In other words, the function

$$\hat{f}_n(\boldsymbol{w}, \boldsymbol{J}, t) = \operatorname{Re} \sum_{k} e^{ik \cdot \boldsymbol{w}} \boldsymbol{E}_k(n, \boldsymbol{J}) \cdot \boldsymbol{z}_k^n(t),$$
(37)

is the perturbed distribution function of those stars that enter (at least once) to the *n*th element. Stars on highly

elongated orbits may visit more than one element. This justifies the summation over n in (34). If an orbit crosses, tangentially or transversally, the boundary of the nth and (n+1)th elements when its phase space coordinates are (w_b, J_b) , the condition $\hat{f}_n(w_b, J_b, t) = \hat{f}_{n+1}(w_b, J_b, t)$ must be fulfilled, which gives

$$\boldsymbol{E}_{k}(n,\boldsymbol{J}_{b})\cdot\boldsymbol{z}_{k}^{n}(t) = \boldsymbol{E}_{k}(n+1,\boldsymbol{J}_{b})\cdot\boldsymbol{z}_{k}^{n+1}(t). \tag{38}$$

To ease this constraint on the elements of $z_k^n(t)$, one can choose the interpolating vector $E_k(n, J)$ so that

$$E_{N_d,k}(n, \mathbf{J}_b) = E_{1,k}(n+1, \mathbf{J}_b),$$
 (39)

$$\begin{cases}
E_{j,k}(n, J_b) = 0, & j < N_d, \\
E_{j,k}(n+1, J_b) = 0, & j > 1,
\end{cases}$$
(40)

and reduce (38) to

$$z_{N_{1},k}^{n}(t) = z_{1,k}^{n+1}(t). (41)$$

Equations (39)–(41) constitute the continuity conditions of the perturbed DF over the ensemble of orbits that migrate between finite elements in the x-space. In §2.4, I will introduce a method to find $E_k(n, J)$.

In order to satisfy $\Sigma_j = \int f_j \mathrm{d}^2 v$, one needs to establish a relation between the functions $\boldsymbol{z}_k^n(t)$ and the nodal densities $\boldsymbol{b}_m^n(t)$. For doing so, I substitute from (8) and (13) into the fundamental equation

$$\Sigma_1(R, \phi, t)R dR d\phi = f_1(\boldsymbol{w}, \boldsymbol{J}, t) d^2 \boldsymbol{J} d^2 \boldsymbol{w}, \tag{42}$$

and use equations (15) and (34) to obtain

$$\sum_{m=-\infty}^{+\infty} \sum_{n=1}^{N} H_n(R) \mathbf{G}_n \cdot \mathbf{b}_m^n(t) e^{\mathrm{i}m\phi} R \, \mathrm{d}R \, \mathrm{d}\phi =$$

$$\sum_{k} \sum_{n=1}^{N} \boldsymbol{E}_{k}(n, \boldsymbol{J}) \cdot \boldsymbol{z}_{k}^{n}(t) e^{\mathrm{i}\boldsymbol{k} \cdot \boldsymbol{w}} \mathrm{d}^{2} \boldsymbol{J} \, \mathrm{d}^{2} \boldsymbol{w}. \tag{43}$$

Taking the inner product of (43) by $H_{n'}(R) G_{n'}^{\mathrm{T}} \exp(-\mathrm{i}m'\phi)$, and carrying out the integrations over the (R, ϕ) and (J, w) spaces, result in the weighted residual form of the fundamental equation as

$$\mathbf{K}(n') \cdot \boldsymbol{b}_{m'}^{n'}(t) = \sum_{k} \sum_{n=1}^{N} H_{n'}(R)$$

$$\times \iint e^{-\mathrm{i}m'\phi} \left[\boldsymbol{G}_{n'}^{\mathrm{T}} \cdot \boldsymbol{E}_{k}(n, \boldsymbol{J}) \right] \cdot \boldsymbol{z}_{k}^{n}(t) e^{\mathrm{i}\boldsymbol{k}\cdot\boldsymbol{w}} \mathrm{d}^{2} \boldsymbol{J} \, \mathrm{d}^{2} \boldsymbol{w}, \qquad (44)$$

where

$$\mathbf{K}(n) = 2\pi \int_{R_{-}}^{R_{n+1}} \mathbf{G}_{n}^{\mathrm{T}}(R) \cdot \mathbf{G}_{n}(R) R dR.$$
 (45)

According to (6), the radial distance $R(t) = \sqrt{x(t) \cdot x(t)}$ and $\exp[i\phi(t)] = [x(t) + iy(t)]/R(t)$ admit Fourier series in terms of \boldsymbol{w} so does the function

$$H_{n'}(R)\boldsymbol{G}_{n'}e^{-\mathrm{i}m'\phi} = \sum_{\boldsymbol{k}'} \boldsymbol{\Psi}_{\boldsymbol{k}'}(m', n', \boldsymbol{J})e^{-\mathrm{i}\boldsymbol{k}'\cdot\boldsymbol{w}}, \tag{46}$$

where the $N_{\rm d} \times 1$ row vector $\mathbf{\Psi}_{k}$ is determined from

$$\Psi_{k}(m',n',\boldsymbol{J}) = \frac{1}{(2\pi)^{2}} \int H_{n'}(R) \boldsymbol{G}_{n'} e^{-im'\phi} e^{i\boldsymbol{k}\cdot\boldsymbol{w}} d^{2}\boldsymbol{w}.$$
(47)

The dependency of the integrand on $H_{n'}(R)$ shows that $\Psi_k(m', n', J)$ is non-zero only for orbits that visit the *n*th

ring element. Our physical sense of (46) is sharpened by summing up its components and setting m=0 to obtain

$$H_n(R) \sum_{i=1}^{N_d} G_{jn}(R) = \sum_{k} \sum_{i=1}^{N_d} \Psi_{j,k}(0, n, \mathbf{J}) e^{-ik \cdot \mathbf{w}}.$$
 (48)

From the properties of interpolating functions in the *R*-domain one can deduce that the summation on the left hand side of (48) is unity. This result and the time-averages theorem (Binney & Tremaine 2008) imply that the quantity

$$\sum_{j=1}^{N_{\rm d}} \Psi_{j,\mathbf{0}}(0, n, \mathbf{J}) = \frac{1}{(2\pi)^2} \int H_n(R) \, \mathrm{d}^2 \mathbf{w}, \tag{49}$$

is the fraction of time that a star of action vector \boldsymbol{J} spends inside the nth element.

Defining

$$\mathbf{D}(\mathbf{k}, m', n', n) = \int \mathbf{\Psi}_{\mathbf{k}}^{\mathrm{T}}(m', n', \mathbf{J}) \cdot \mathbf{E}_{\mathbf{k}}(n, \mathbf{J}) \, \mathrm{d}^{2}\mathbf{J}, \tag{50}$$

and substituting from (46) into (44) lead to

$$\boldsymbol{b}_{m'}^{n'}(t) = 4\pi^2 \sum_{k} \sum_{n=1}^{N} \left[\mathbf{K}^{-1}(n') \cdot \mathbf{D}(k, m', n', n) \right] \cdot \boldsymbol{z}_{k}^{n}(t), \quad (51)$$

which determines the vector of nodal densities in terms of $\mathbf{z}_k^n(t)$. Taking into account the constraints (41) and collecting the components of $\mathbf{z}_k^n(t)$ (for $n=1,2,\cdots,N$) in a single vector $\mathbf{z}_k(t)$, and combining the system of linear equations (51) for all ring elements in the configuration space, result in

$$\mathbf{d}_{m}(t) = \sum_{k} \mathbf{F}(\mathbf{k}, m) \cdot \mathbf{z}_{k}(t), \tag{52}$$

where $\mathbf{F}(\mathbf{k},m)$ is an $N_{\rm t} \times N_{\rm t}$ square matrix. Let me define $\mathbf{L}(\mathbf{k},m) = \mathbf{C}(m) \cdot \mathbf{F}(\mathbf{k},m)$. Equations (30) and (52) will self-consistently give the nodal potentials $\mathbf{p}_m(t)$ in terms of $\mathbf{z}_{\mathbf{k}}(t)$:

$$\boldsymbol{p}_{m}(t) = \sum_{\boldsymbol{k}} \mathbf{L}(\boldsymbol{k}, m) \cdot \boldsymbol{z}_{\boldsymbol{k}}(t). \tag{53}$$

By equating (12) and (10), and applying (14) and (46), I conclude that

$$\tilde{h}_{1,k}(\boldsymbol{J},t) = \sum_{m=-\infty}^{+\infty} \sum_{n=1}^{N} \boldsymbol{\Psi}_{-k}(-m,n,\boldsymbol{J}) \cdot \boldsymbol{a}_{m}^{n}(t).$$
 (54)

This means that a star of the angle-action coordinates (w, J) will experience the perturbed self-gravitational potential field

$$\hat{h}_n(\boldsymbol{w}, \boldsymbol{J}, t) = \operatorname{Re} \sum_{m=-\infty}^{+\infty} \sum_{\boldsymbol{k}} e^{i\boldsymbol{k}\cdot\boldsymbol{w}} \boldsymbol{\Psi}_{-\boldsymbol{k}}(-m, n, \boldsymbol{J}) \cdot \boldsymbol{a}_m^n(t), \quad (55)$$

during its passage through the nth element. Consequently, the perturbed Hamiltonian associated with the stars that enter to the nth element becomes

$$\hat{\mathcal{H}}_n(\boldsymbol{w}, \boldsymbol{J}, t) = \operatorname{Re}\left[\hat{h}_n(\boldsymbol{w}, \boldsymbol{J}, t) + \sum_{\boldsymbol{k}} \tilde{h}_{e, \boldsymbol{k}}(\boldsymbol{J}, t) e^{i\boldsymbol{k}\cdot\boldsymbol{w}}\right].$$
 (56)

2.3 Galerkin weighting of the linearised CBE

Given the functions \hat{f}_n , \hat{h}_n and $\Phi_{\rm e}$ in the angle-action space, the CBE reads

$$\sum_{n=1}^{N} \left\{ \frac{\partial \hat{f}_{n}}{\partial t} + \left[f_{0}, \hat{h}_{n} \right] + \left[\hat{f}_{n}, \mathcal{H}_{0} \right] \right\} + \left[f_{0}, \Phi_{e} \right] =$$

$$- \sum_{n=1}^{N} \left[\hat{f}_{n}, \Phi_{e} \right] - \sum_{n,n'=1}^{N} \left[\hat{f}_{n}, \hat{h}_{n'} \right].$$
(57)

In the present analysis, the higher-order terms $[\hat{f}_n, \hat{h}_{n'}]$ and $[\hat{f}_n, \Phi_e]$ are ignored. On substituting from (37) and (56) into (57), taking the inner product of the resulting equation with $\exp(-i\mathbf{k}'\cdot\mathbf{w})\mathbf{E}_{\mathbf{k}'}^{\mathrm{T}}(n',\mathbf{J})$ and integrating over \mathbf{w} and \mathbf{J} , the following system of ordinary differential equations

$$\mathrm{i} \sum_{n=1}^{\infty} \mathbf{E}_1(n',n,\mathbf{k}') \cdot \frac{\mathrm{d}}{\mathrm{d}t} \mathbf{z}_{\mathbf{k}'}^n(t) = \sum_{n=1}^{\infty} \mathbf{E}_2(n',n,\mathbf{k}') \cdot \mathbf{z}_{\mathbf{k}'}^n(t)$$

$$-\mathbf{Z}_{n'}(\mathbf{k}',t) - \sum_{n=1}^{\infty} \sum_{m=-\infty}^{+\infty} \mathbf{E}_3(m,n',n,\mathbf{k}') \cdot \mathbf{a}_m^n(t), \qquad (58)$$

are obtained for $n' = 1, 2, \dots, N$ so that

$$\mathbf{E}_{1} = \int \mathbf{E}_{k}^{\mathrm{T}}(n', \mathbf{J}) \cdot \mathbf{E}_{k}(n, \mathbf{J}) \, \mathrm{d}^{2} \mathbf{J}, \tag{59}$$

$$\mathbf{E}_{2} = \int (\mathbf{k} \cdot \mathbf{\Omega}) \, \mathbf{E}_{k}^{\mathrm{T}}(n', \mathbf{J}) \cdot \mathbf{E}_{k}(n, \mathbf{J}) \, \mathrm{d}^{2} \mathbf{J}, \tag{60}$$

$$\mathbf{E}_{3} = \int \left(\mathbf{k} \cdot \frac{\partial f_{0}}{\partial \mathbf{J}} \right) \mathbf{E}_{\mathbf{k}}^{\mathrm{T}}(n', \mathbf{J}) \cdot \mathbf{\Psi}_{-\mathbf{k}}(-m, n, \mathbf{J}) d^{2} \mathbf{J}, \quad (61)$$

$$\mathbf{Z}_{n'} = \int \left(\mathbf{k} \cdot \frac{\partial f_0}{\partial \mathbf{J}} \right) \mathbf{E}_{\mathbf{k}}^{\mathrm{T}}(n', \mathbf{J}) \tilde{h}_{e, \mathbf{k}}(\mathbf{J}, t) \, \mathrm{d}^2 \mathbf{J}.$$
 (62)

The matrices \mathbf{E}_1 , \mathbf{E}_2 and \mathbf{E}_3 have the dimension $N_{\rm d} \times N_{\rm d}$, and the forcing term $\mathbf{Z}_{n'}(\mathbf{k},t)$ is a column vector of dimension $N_{\rm d}$. The integrals in (59)–(62) are performed over a \mathbf{J} -subspace whose orbits visit both the n'th and nth elements. The summation over n in (58) shows a coupling between adjacent and also unconnected distant elements, which communicate their dynamical information through elongated orbits. For example, if two peaks of a density wave lie on a given trajectory, deformation of that trajectory near one peak will influence its behaviour near the other one. Longrange interactions of this kind will be negligible in models populated by near-circular orbits, or when density perturbations rise and fall in harmony with the equilibrium density profile. In such conditions, one can keep in (58) only the terms of n=n' and write

$$i\mathbf{E}_{1}(n, \mathbf{k}') \cdot \frac{\mathrm{d}}{\mathrm{d}t} \mathbf{z}_{\mathbf{k}'}^{n}(t) = \mathbf{E}_{2}(n, \mathbf{k}') \cdot \mathbf{z}_{\mathbf{k}'}^{n}(t)$$
$$-\mathbf{Z}_{n}(\mathbf{k}', t) - \sum_{m = -\infty}^{+\infty} \mathbf{E}_{3}(m, n, \mathbf{k}') \cdot \mathbf{a}_{m}^{n}(t). \tag{63}$$

This is indeed the weighted residual form of the linearised CBE over the nth element:

$$\frac{\partial \hat{f}_n}{\partial t} + \left[f_0, \hat{\mathcal{H}}_n \right] + \left[\hat{f}_n, \mathcal{H}_0 \right] = 0, \tag{64}$$

with Poisson brackets taken over a phase subspace whose stars visit the nth element. The set of element CBEs are sufficient (but not necessary) conditions for the global equation (57) to be satisfied. I recommend the application of the Galerkin form (63) to the modelling of minimally peaked

waves like the one displayed in the top-right panel of Figure 2.

Dropping the prime sign for brevity, and assembling either the system of equations (58) or (63) result in

$$\mathbf{U}_{1}(\mathbf{k}) \cdot \frac{\mathrm{d}\mathbf{z}_{k}(t)}{\mathrm{d}t} = -\mathrm{i}\mathbf{U}_{2}(\mathbf{k}) \cdot \mathbf{z}_{k}(t) + \mathrm{i}\mathbf{Z}(\mathbf{k}, t) + \sum_{m=-\infty}^{+\infty} \mathrm{i}\mathbf{U}_{3}(\mathbf{k}, m) \cdot \mathbf{p}_{m}(t),$$

$$(65)$$

where \mathbf{U}_1 , \mathbf{U}_2 and \mathbf{U}_3 are $N_{\rm t} \times N_{\rm t}$ square matrices, the forcing function $\mathbf{Z}(\mathbf{k},t)$ is a column vector of dimension $N_{\rm t}$, and the vector of nodal potentials $\mathbf{p}_m(t)$ is computed from (53). The continuity conditions (41) must be taken into account in the assembly process. It is therefore a standard procedure to integrate the linear system (65) over the time domain and monitor the evolution of $\tilde{f}_{1,k}(\mathbf{J},t)$.

In the absence of external perturbations, equation (65) admits a solution of the form $z_k(t) = \exp(-i\omega t)\zeta_k$ and it is reduced to the following linear eigensystem:

$$\sum_{m=-\infty}^{+\infty} \sum_{\mathbf{k}'} \left[\mathbf{U}_3(\mathbf{k}, m) \cdot \mathbf{L}(\mathbf{k}', m) \right] \cdot \zeta_{\mathbf{k}'} = \left[\mathbf{U}_2(\mathbf{k}) - \omega \mathbf{U}_1(\mathbf{k}) \right] \cdot \zeta_{\mathbf{k}} , \tag{66}$$

that can be solved for the eigenfrequency ω and its corresponding eigenvector (mode shape) ζ_k using standard numerical packages. The general form of the eigensystem presented in (66) applies to initially non-axisymmetric discs that host a rich family of orbits living on resonant bundles. In the limit of initially round systems, only rosette orbits fill the phase space and it is convenient to define the generalised momenta of a test star by $(p_1, p_2) = (\dot{R}, R^2 \dot{\phi})$. The vector of action variables $\mathbf{J} = (J_1, J_2)$ is then calculated from the integrals

$$J_1 = \frac{1}{2\pi} \oint p_1 dR, \quad J_2 = \frac{1}{2\pi} \oint p_2 d\phi,$$
 (67)

along the rosette orbits of angular momentum $L=p_2$ and energy E so that

$$E \equiv \mathcal{H}_0(\mathbf{J}) = \frac{1}{2} \left(p_1^2 + \frac{p_2^2}{R^2} \right) + \Phi_0(R). \tag{68}$$

The angle variables $\mathbf{w} = (w_1, w_2)$ conjugate to the actions (J_1, J_2) evolve according to the linear law $w_i = \Omega_i t + w_i(0)$ (i=1,2) with $\Omega_i = \partial \mathcal{H}_0/\partial J_i$. The axisymmetry condition implies $\Psi_{-k}(-m, n, \mathbf{J}) = \Psi_k(m, n, \mathbf{J})$ and

$$\Psi_{(k_1,k_2)}(m,n,\mathbf{J}) = 0, \text{ if } k_2 \neq m.$$
 (69)

Consequently, the summation over m is dropped in (65)–(66), and the governing equations are decoupled for different values of the wavenumber m. The spectrum of the eigenfrequency ω contains pure oscillatory (van Kampen) modes as well as unstable ones. Spurious eigenfrequencies may also appear in the spectrum due to finite element discretisation errors. Such cases can be rejected by investigating their corresponding mode shapes.

2.4 Interpolating functions in the action space

The choice of the row vector $E_k(n, J)$ has a remarkable effect on the performance of the FEM. A somewhat trivial

approach is to identify the sub-domain of J-space whose orbits visit the nth element, and generate a finite element mesh in that sub-domain by setting $E_{i,k}(n,J)$ to elementary two dimensional counterparts of the functions used in §2.1. This procedure, however, is not computationally efficient because it increases the sizes of global matrices \mathbf{L} and \mathbf{U}_i (i=1,2,3). Below, I follow an alternative approach and show that the neutral solutions of (64) can perform as suitable interpolating functions.

In the absence of external disturbances and assuming $\mathbf{z}_{k}^{n} = \exp(-\mathrm{i}\omega t)\zeta_{k}^{n}$, equation (64) gives the exact relation

$$\boldsymbol{E}_{k}(n,\boldsymbol{J})\cdot\zeta_{k}^{n} = \left(\frac{\boldsymbol{k}\cdot\frac{\partial f_{0}}{\partial \boldsymbol{J}}}{\boldsymbol{k}\cdot\boldsymbol{\Omega}-\omega}\right)\sum_{m=-\infty}^{+\infty}\boldsymbol{\Psi}_{-k}(-m,n,\boldsymbol{J})\cdot\boldsymbol{a}_{m}^{n}. \quad (70)$$

Denoting $\langle a|b\rangle$ as the inner product of the vectors a and b, one can derive the following identity

$$E_{k}(n, \mathbf{J})\langle \zeta_{k}^{n} | \zeta_{k}^{n} \rangle = \left(\mathbf{k} \cdot \frac{\partial f_{0}}{\partial \mathbf{J}} \right) (\mathbf{k} \cdot \mathbf{\Omega} - \omega)^{-1}$$

$$\times \sum_{m=-\infty}^{+\infty} \mathbf{\Psi}_{-k}(-m, n, \mathbf{J}) \langle \mathbf{a}_{m}^{n} | \zeta_{k}^{n} \rangle.$$
 (71)

Without loss of generality, I choose ζ_k^n so that $\langle \zeta_k^n | \zeta_k^n \rangle$ is normalised to unity, and take the $\omega \to 0$ limit of (71) to obtain a class of interpolating vectors $\mathbf{E}_k(n, \mathbf{J})$.

To determine the constant coefficients $\langle a_n^n | \zeta_k^n \rangle$, I set $\omega = 0$ and substitute from (70) into (43). The weighted residual form of the resulting equation becomes:

$$\mathbf{K}(n') \cdot \boldsymbol{b}_{m'}^{n'} = (2\pi)^2 \sum_{m=-\infty}^{+\infty} \sum_{n=1}^{N} \left[\sum_{k} \right] \times \int \frac{\boldsymbol{k} \cdot \frac{\partial f_0}{\partial \boldsymbol{J}}}{\boldsymbol{k} \cdot \boldsymbol{\Omega}} \boldsymbol{\Psi}_{k}^{\mathrm{T}}(m', n', \boldsymbol{J}) \cdot \boldsymbol{\Psi}_{-k}(-m, n, \boldsymbol{J}) \, \mathrm{d}^2 \boldsymbol{J} \cdot \boldsymbol{a}_{m}^{n}, (72)$$

for $n'=1,2,\cdots,N$ and $m'\in(-\infty,+\infty)$. Assembling this system of matricial equations and combining it with (30) yield

$$\mathbf{p}_{m'} = \sum_{m=-\infty}^{+\infty} \tilde{\mathbf{S}}(m', m) \cdot \mathbf{p}_m \iff \mathbf{I} \cdot \mathbf{p} = \mathbf{S} \cdot \mathbf{p},$$

$$\mathbf{p} = \begin{bmatrix} \cdots & \mathbf{p}_{-2}^{\mathrm{T}} & \mathbf{p}_{-1}^{\mathrm{T}} & \mathbf{p}_{0}^{\mathrm{T}} & \mathbf{p}_{+1}^{\mathrm{T}} & \mathbf{p}_{+2}^{\mathrm{T}} & \cdots \end{bmatrix}^{\mathrm{T}},$$
(73)

where \mathbf{I} is the identity matrix and the constant $N_{\rm t} \times N_{\rm t}$ matrices $\tilde{\mathbf{S}}(m',m)$ constitute the blocks of \mathbf{S} . A non-trivial solution of (73) for p, which will lie in the nullspace of $\mathbf{I} - \mathbf{S}$, can be obtained by singular value decomposition of $\mathbf{I} - \mathbf{S}$ (see Press et al. 2001). Consequently, one can compute $\langle a_m^n | \zeta_k^n \rangle$ and fully determine the interpolating vector. I remark that some resonant orbits can contribute a singularity to $E_k(n,J)$ when $k \cdot \Omega \approx 0$, but such a singularity is integrable. Initially axisymmetric discs satisfy the condition (69) and the interpolating vector reads

$$E_{k}(n, \mathbf{J}) = \left(k \cdot \frac{\partial f_{0}}{\partial \mathbf{J}}\right) (k \cdot \Omega)^{-1} \Psi_{-k}(-m, n, \mathbf{J}), \tag{74}$$

which has been used throughout this paper. Using (46) one can verify that the elements of $\Psi_k(m,n,J)$ satisfy the continuity conditions (39) and (40), so do the interpolating functions.

Finite Element Zang-Toomre mode N $N_{\rm d}$ Discretisation Rule $(\Omega_{\rm p}, s)$ $M_{\rm in}$ $(\Omega_{\rm p}, s)$ $R_n = -3\ln u_n$ Α 4 10 2 (0.450, 0.189)(0.439, 0.127)A 4 20 2 $R_n = -2\ln u_n$ (0.444, 0.137)(0.439, 0.127) $R_n = -1.5 \ln u_n$ Α 4 75 2 (0.442, 0.127)(0.439, 0.127) $R_n = -1.5 \ln u_n$ Α 16 2 (0.486, 0.316)(0.482489, 0.321296)75 $R_n = -1.5 \ln u_n$ В 75 2 (0.395, 0.168)(0.386203, 0.171397)16 \mathbf{C} 16 $R_n = -1.5 \ln u_n$ (1.180, 0.162)(1.161724, 0.154866) $R_n = 2(1 - u_n)/u_n$ Α 4 50 3 (0.43960, 0.12675)(0.439426, 0.127181)

Table 1. Eigenfrequencies of the cutout Mestel discs for m=2.

3 SOLVED EXAMPLES

To show the power of the FEM, I solve two problems regarding the dynamics of disc galaxies and spiral structure formation. As my first case study, I investigate the stability of the cutout stellar Mestel disc (Zang 1976; Toomre 1977; Evans & Read 1998a,b). I have chosen this model because its shallow density falloff (like R^{-1}) fuels growing perturbations over a large radial distance from the galactic centre, and the methods that rely on basis function expansions (Kalnajs 1977; Jalali & Hunter 2005; Jalali 2007) require too many terms to guarantee the convergence of the associated eigenvalue problem. The second problem studied here is the disturbances induced by a satellite galaxy on its initially axisymmetric primary. The satellite galaxy is assumed to live inside the same dark matter halo of the primary, and it moves on a rosette orbit, coplanar with the primary's disc.

3.1 Stability of the stellar Mestel disc

The equilibrium surface density and its associated self-gravitational potential of the Mestel disk are given, respectively, by (Evans & Read 1998a)

$$\Sigma_0(R) = \Sigma_s \left(\frac{R_0}{R}\right), \tag{75}$$

$$\Phi_0(R) = v_0^2 \ln\left(\frac{R}{R_0}\right), \quad v_0^2 = 2\pi G \Sigma_s.$$
(76)

Here, Σ_s is a normalising factor, R_0 is a length scale, and v_0 is the (constant) velocity of stars on circular orbits. The space of the orbital frequencies (Ω_1, Ω_2) of the Mestel disc is an angular sector that extends to infinity due to the singularity of the gravitational force as $R \to 0$. The lower and upper boundaries of the frequency space are the straight lines $\Omega_2 = \Omega_1/2$ and $\Omega_2 = \Omega_1/\sqrt{2}$ that correspond to radial and circular orbits, respectively.

I follow Zang (1976) and Evans & Read (1998a), and use the equilibrium DF:

$$f_0(E, L) = \frac{\sum_s (\gamma + 1)^{1+\gamma/2}}{2^{\gamma/2} \sqrt{\pi} R_0^{\gamma} v_0^{\gamma+2} \Gamma\left[\frac{1}{2} (\gamma + 1)\right]} L^{\gamma} e^{-(\gamma + 1)E/v_0^2}, (77)$$

and the cutout DFs derived from that as

$$f_{\text{cut}}(E, L) = f_0(E, L) \frac{L^{M_{\text{in}}}}{[L^{M_{\text{in}}} + (R_0 v_0)^{M_{\text{in}}}]},$$
 (78)

where the integer exponent $M_{\rm in}$ specifies the sharpness of

the inner cutout. The cutout DF introduced in (78) means that stars with $L \ll R_0 v_0$ will not participate in density perturbations though they can still contribute to the mean-field gravitational potential.

I set $R_0=v_0=G=1$ and choose a model with $(M_{\rm in}, \gamma)=(4,6)$. Since most perturbations decay monotonically as $R \to \infty$, it is useful to adopt a nonuniform mesh so that the widths of elements decrease towards the disc centre. I divide the configuration space to N finite ring elements and apply either of the following rules

$$R_n = -\alpha_1 \ln u_n, \quad R_n = \alpha_2 \frac{1 - u_n}{u_n},\tag{79}$$

to generate elements of nonuniform width where

$$u_n = 1 - \frac{1}{2(N+1)} - \frac{n-1}{N+1}, \quad n = 1, 2, \dots, N+1.$$
 (80)

All integrals over the action space are evaluated after carrying out three successive changes of variables as

$$(J_1, J_2) \rightarrow (E, L) \rightarrow (R_{\min}, R_{\max}) \rightarrow (R_c, e).$$
 (81)

Here R_{\min} and R_{\max} are the minimum and maximum galactocentric distances of rosette orbits and

$$R_{\min} = R_c(1-e), R_{\max} = R_c(1+e), 0 \le e \le 1.$$
 (82)

For axisymmetric discs, the Fourier numbers $\mathbf{k} = (k_1, k_2)$ contract to $k_1 = 0, \pm 1, \pm 2, \cdots$ and $k_2 = m$, which substantially decreases the size of the eigensystem (66). Nevertheless, one must truncate the Fourier series in terms of the radial angle w_1 . Taking $-10 \le k_1 \le 10$ suffices in most systems (e.g., Jalali & Hunter 2005). The eigenfrequencies and their corresponding eigenvectors of equation (66) are computed using the same algorithms and subroutines of Jalali (2007).

Top row in Figure 2 shows the fastest growing bisymmetric mode A of m=2, which has been obtained using the Galerkin form (63) and through solving (66) for different finite element gridings by taking $-2 \le k_1 \le 5$. The pattern speed Ω_p and growth rate s of this mode (note: $\omega = m\Omega_p + is$) are given in Table 1 up to three decimal places, and they are compared with the values computed by Zang (1976) and also reported in Toomre (1977). It is evident that the FEM with $(N, \alpha_1) = (75, 1.5)$ has given a satisfactory accuracy of 0.6%. By increasing the number of ring elements the mode shape is smoothened too. I have also utilised (58) and computed the eigenfrequency spectrum of a model with $(M_{\rm in}, \gamma) = (16, 6)$. The spectrum includes three

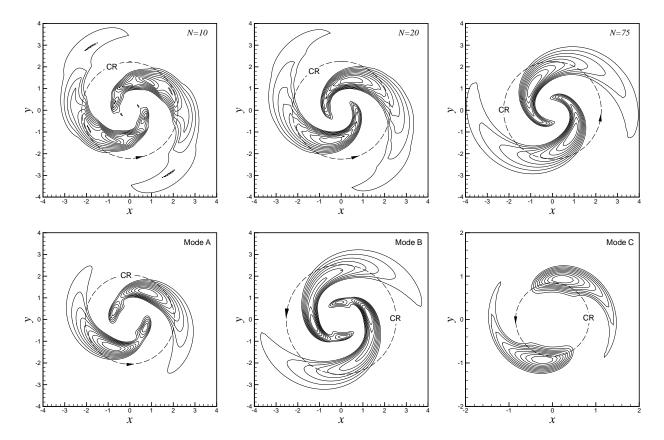


Figure 2. Top row: The fundamental unstable mode A of the cutout Mestel disk with $M_{\rm in}=4$, $N_{\rm d}=2$ and $\gamma=6$. Left, middle and right figures correspond to $(N,\alpha_1)=(10,3)$, $(N,\alpha_1)=(20,2)$ and $(N,\alpha_1)=(75,1.5)$, respectively. It is evident that increasing the number of ring elements smoothens the density isocontours. This mode has also been displayed in Figure 12 of Toomre (1977). Bottom row: Modes A, B and C of the cutout Mestel disc with $(M_{\rm in},\alpha_1)=(16,1.5)$, N=75 and $\gamma=6$. Mode C is an inner edge mode that develops where the cutout surface density has a rising profile versus R. In all figures, positive isodensity contours of $\Sigma_1(R,\phi,0)$ have been plotted from 10% to 90% of the maximum, with the steps of 10%. Dashed circles mark the location of the corotation resonance (CR).

prominent modes A, B and C, which have been found with an average error of 2% (see Table 1). Mode C is an inner edge mode that comes into existence due to sharp cutout. The eigenfrequencies of all these modes have been known to Alar Toomre up to six decimal places (private communication; see Table 1) and I have demonstrated their corresponding mode shapes in the bottom row of Figure 2. They have not already been displayed in the literature.

The accuracy of FEM calculations is determined by several factors: (i) element types, interpolation rule and the degree of differentiability at the nodes (ii) the number of Fourier terms in the w_1 -direction (iii) the number of ring elements and their sizes specified by ΔR_n (iv) the precision of the integrals taken over the action space in constructing the matrices L, E_1 , E_2 and E_3 (v) the accuracy of eigenvalue solver. Furthermore, not all eigenmodes will have the same precision because their clumps do not simultaneously fall in a region with appropriate number of elements. For instance, the growth rate of mode C is less accurate than modes A and B, and the pattern speeds of all modes have been overestimated. These errors correlate mainly with the type and sizes of elements. Using the discretisation rule $R_n = 2(1 - u_n)/u_n$, which increases the radius of the outermost element, and by applying quadratic

elements ($N_{\rm d}=3$), the accuracy of ($\Omega_{\rm p},s$) for mode A of the model with $M_{\rm in}=4$ reaches to an impressive level of ($\pm 0.0002, \pm 0.0004$) even by taking N=50 elements. Last row in Table 1 compares the eigenfrequency found by FEM with Alar Toomre's recent high-precision results. Although an adaptive mesh refinement can enhance the accuracy of an individual mode (if not the whole spectrum), a significant improvement is anticipated only by a C_1 finite element formulation that assures the smoothness of perturbed quantities over the entire configuration and phase spaces.

3.2 Perturbations induced by a satellite galaxy

Kinematics and dynamics of galaxies are highly influenced by their environment. Mergers, close encounters, and bound companions determine the structure and evolution of most cluster galaxies. The FEM developed in this study is capable of modelling the disturbances of complex interactions between stellar systems, and it can complement N-body simulations in the modeling of multi-scale structure formation and evolution of galaxies. As an illustrative example, I apply the FEM and investigate the induced disturbances of a stellar disc by a distant satellite galaxy. The primary stellar disc is assumed to be a doubly cutout Mestel disc with the

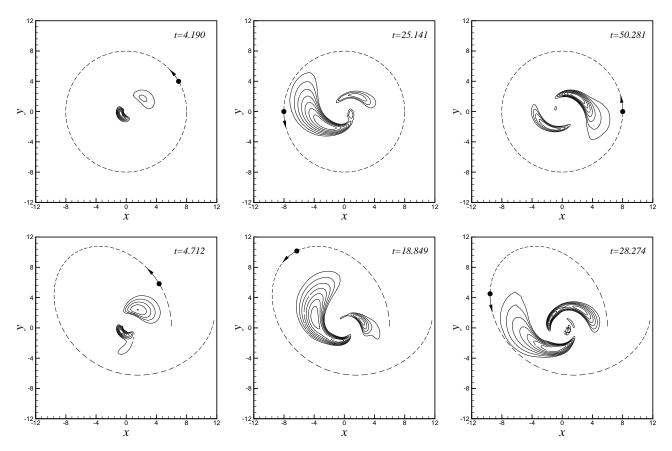


Figure 3. Disturbances induced by a satellite galaxy (filled circle) on a stable doubly cutout Mestel disc. Top row: The satellite moves on a circular orbit of radius $R_{\rm S}=8$. Bottom row: Satellite's orbit is a rosette of $R_{\rm min}=6$ and $R_{\rm max}=12$. The initial azimuth $\phi_{\rm S}(0)$ of the perturber is zero. This state of the system also defines the origin of time: t=0. Only positive isodensity contours of $\Sigma_1(R,\phi,t)$ have been plotted from 30% to 90% of the maximum, with the steps of 10%.

DF

$$f_{\text{cut}}(E, L) = \frac{\beta f_0(E, L) L^{M_{\text{in}}} L_c^{M_{\text{out}}}}{[L^{M_{\text{in}}} + (R_0 v_0)^{M_{\text{in}}}] [L^{M_{\text{out}}} + L_c^{M_{\text{out}}}]},$$
(83)

where $0 < \beta \le 1$, and f_0 has been defined in (77). Immobilised particles with $L \ll R_0 v_0$ and $L \gg L_c$ simulate, respectively, a hot bulge and a rigid dark halo. Unstable modes are indeed the homogeneous solutions of equation (65). By adjusting β and the set of parameters $(L_c, M_{\rm in}, M_{\rm out})$, one can build a stable axisymmetric disc and study only the effect of the external perturber as the particular solutions of (65).

I make two simplifying assumptions for the motion of the satellite galaxy: (i) the dynamical friction of both the baryonic and dark matter components is ignored (ii) the satellite galaxy is a point mass that keeps moving on a rosette orbit while its motion is governed by the same massive dark halo that hosts the primary. One can therefore neglect the indirect gravitational force of the satellite galaxy on the disc stars and write the disturbance function as

$$\Phi_{\rm e}(R,\phi,t) = -\frac{GM_{\rm S}}{R_{\rm S}} \sum_{i=0}^{\infty} \left(\frac{R}{R_{\rm S}}\right)^i P_i^0 \left[\cos(\phi - \phi_{\rm S})\right], \tag{84}$$

where $[R_{\rm S}(t),\phi_{\rm S}(t)]$ are the polar coordinates of a satellite (of mass $M_{\rm S}$) measured with respect to a non-rotating frame whose origin is attached to the primary's centre. The po-

tential field of the rigid dark halo is logarithmic at distant regions. Thus, the motion of the satellite is governed by

$$\frac{\mathrm{d}^2 R_\mathrm{S}}{\mathrm{d} t^2} - R_\mathrm{S} \left(\frac{\mathrm{d} \phi_\mathrm{S}}{\mathrm{d} t} \right)^2 = -\frac{v_0^2}{R_\mathrm{S}}, \quad \frac{\mathrm{d}}{\mathrm{d} t} \left[R_\mathrm{S}^2 \left(\frac{\mathrm{d} \phi_\mathrm{S}}{\mathrm{d} t} \right) \right] = 0. \quad (85)$$

To implement the FEM, one needs to represent the disturbance function in terms of the angle-action variables. I define

$$X_{1,k_1}(\mathbf{J}) = \frac{1}{2\pi} \oint R \cos[k_1 w_1 + (w_2 - \phi)] \, \mathrm{d}w_1, \tag{86}$$

$$Y_{j,k_1}(\mathbf{J}) = \frac{1}{2\pi} \oint R^2 \cos[k_1 w_1 + j(w_2 - \phi)] dw_1,$$
 (87)

and keep the leading i < 2 terms of (84) to obtain

$$\Phi_{e}(\boldsymbol{w}, \boldsymbol{J}, t) \approx \operatorname{Re} \left[-\frac{GM_{S}}{R_{S}} - \frac{GM_{S}}{4R_{S}^{3}} \sum_{k_{1} = -\infty}^{+\infty} Y_{0, k_{1}}(\boldsymbol{J}) e^{ik_{1}w_{1}} \right. \\
\left. - \frac{GM_{S}}{R_{S}^{2}} \sum_{k_{1} = -\infty}^{+\infty} e^{-i\phi_{S}} X_{1, k_{1}}(\boldsymbol{J}) e^{i(k_{1}w_{1} + w_{2})} \\
\left. - \frac{3GM_{S}}{4R_{S}^{3}} \sum_{k_{1} = -\infty}^{+\infty} e^{-2i\phi_{S}} Y_{2, k_{1}}(\boldsymbol{J}) e^{i(k_{1}w_{1} + 2w_{2})} \right]. (88)$$

The first term on the right hand side of (88) can be dropped because it does not contribute to the disturbing force. The second term generates an unsteady, axisymmetric, particular solution of (65). The third and fourth terms excite, respectively, rotating patterns of angular wavenumbers m=1 and m=2. Since I am considering the linearised CBE, all solutions will be superposed to get the imposed perturbed density.

To this end, I adopt the Galerkin form (63) and set the model parameters to $v_0 = R_0 = G = 1$, $\gamma = 6$, $\beta = 0.1$, $L_c = 4$, and $M_{\rm in} = M_{\rm out} = 2$, which result in a disc of active mass $M_{\rm disc}=0.417$ in the normalised units. My calculations using the eigensystem (66) shows that this disc is stable to internal excitation of any angular wavenumber m. It is therefore guaranteed that in the presence of an external perturber, the disc will not develop an exponentially growing mode. I assume $GM_S = 0.04$, generate a non-uniform grid of $(N, \alpha_1) = (75, 2)$, and keep the terms corresponding to the radial Fourier numbers $-5 \le k_1 \le +5$. Since I have taken only the first three terms of the disturbance function (0 < i < 2), there will be 3×11 unknown vectors of the amplitude functions $z_k(t)$, each being a 76 × 1 column vector. I turn on the forcing vector $\mathbf{Z}(\mathbf{k},t)$ when the satellite's true anomaly is $\phi_{\rm S}=0$ at the origin of time (t=0), and integrate equations (65) by an accuracy of 10^{-4} using the subroutine ODEINT of Press et al. (2001).

Top row in Figure 3 displays three snap shots of generated spiral arms as the satellite moves on a circular orbit of radius $R_{\rm S}=8$. The fundamental feature of density perturbations is that the closer spiral arm to the perturber is more extensive than the arm on the opposite side. This shows the dominance of the i=1 term in (84). Bottom row in Figure 3 demonstrates the density perturbations induced by the same satellite of $GM_{\rm S}=0.04$, but orbiting on a rosette of $R_{\min} = 6$ and $R_{\max} = 12$. It is evident that the spiral arm opposite to the satellite's location is amplified as the satellite descends from its orbital apocentre. For both the circular and rosette orbits, the major wave packets of density perturbations lead the satellite. This phase lead increases as the time is elapsed, but it is more prominent (even more than 90°) when the satellite's orbit is highly eccentric. The results are not altered by taking $-8 \le k_1 \le +8$, which shows a fast convergence of Fourier series in terms of w_1 .

4 CONCLUSIONS

I modelled the dynamics of collisionless stellar systems using finite elements and used the FEM to study the spiral structure formation. The method is highly adaptable to all given initial density profiles, and it can be applied to stability problems as well as disturbances induced by external sources. The FEM converges by taking a relatively small number of radial elements and it can accurately resolve different growing modes of unstable discs. Although the examples of this study were confined to the perturbations of axisymmetric discs, the derived equations are quite general and can be readily applied to elongated discs with rich orbital structures.

Applying a Fourier expansion in the azimuthal ϕ -direction is favoured in theoretical studies of toy galaxy models. In real systems one may need too many Fourier terms to get converged the perturbed density and its corresponding potential. This problem can be avoided by using a two dimensional finite element grid in the (R, ϕ) -space, instead of ring elements only in the radial direction.

Two dimensional elements can be triangular, rectangular or mapped ones depending on the shape of the galaxy. Moreover, a two dimensional grid makes the governing equations independent of the wavenumber m, and simplifies the form of projected equations.

For models with N < 100 ring elements, and for radial Fourier numbers in the range $-10 \le k_1 \le 10$, the largest size of ordinary differential equation that must be integrated to study the pattern evolution, is of $\mathcal{O}(10^3)$. This is far less than motion equations solved in N-body simulations of typical disc galaxies. Given the accuracy of results that I obtained for the global modes of the cutout Mestel disc, the FEM can thus be regarded as an extremely efficient technique as long as the integrator of evolutionary equations is concerned. However, the spectral analysis of orbit families and the calculation of the row vector $\Psi_{-k}(-m,n,J)$ is costly. This makes the numerical effort of the FEM comparable with Schwarzschild's (1979) method because one needs to identify and analyse the orbits that visit each element.

The error of FEM simulations can be controlled not necessarily by increasing the number of elements, but by suitable (adaptive) variation of element sizes and increasing the order of interpolating functions. Perhaps the most remarkable advantage of the FEM is that it can be directly linked with computational fluid dynamics codes, which mainly use finite difference and finite element methods, to study the co-evolution of the stellar and gas components of galaxies. The elements of a compound medium does not evolve according to the same (or similar) physical principles, but a common simulation method can make a fruitful bridge between them. For instance, the FEM modeling of the stellar and gas components may provide a better understanding of the starburst activity in spiral arms. The reliance of FEM on matrix algebra also distinguishes it from other simulation methods. Since matrix summations and products are performed on graphic cards more efficient than CPU, commercial hardwares in the PC market can be used to build special-purpose computer boards for the FEM simulations of complex stellar systems.

ACKNOWLEDGEMENTS

I express my sincere thanks to Alar Toomre for his illuminating discussions and for providing me with his new high-precision results of Zang's disc. I also thank the anonymous referee for a useful report. This work was partially supported by the Research Vice-Presidency at Sharif University of Technology.

REFERENCES

Agertz O., Moore B., Stadel J., Potter D. et al., MNRAS, 380, 963

Binney J., Tremaine S., 2008, Galactic Dynamics. 2nd edition, Princeton University Press, Princeton

Clutton-Brock M., 1972, Ap&SS, 16, 101

Clutton-Brock M., 1973, Ap&SS, 23, 55

Evans N.W., Read J.C.A., 1998a, MNRAS, 300, 83

Evans N.W., Read J.C.A., 1998b, MNRAS, 300, 106

Gaburov E., Harfst S., Portegies Zwart S., 2009, New Astronomy, 14, 630

Hernquist L., Ostriker J.P., 1992, ApJ, 386, 375

Jalali M.A., Hunter C., 2005, ApJ, 630, 804

Jalali M.A., 2007, ApJ, 669, 218

Kaasalainen M., Binney J., 1994a, PRL, 73(18), 2377

Kaasalainen M., Binney J., 1994b, MNRAS, 268, 1033

Kalnajs A.J., 1976, ApJ, 205, 745

Kalnajs A.J., 1977, ApJ, 212, 637

Lewis R.W., Nithiarasu P., Seetharamu K.N., 2004, Fundamentals of the Finite Element Method for Heat and Fluid Flow, John Wiley & Sons, West Sussex, England

Makino J., Fukushige T., Koga M., Namura K., 2003, PASJ, 55, 1163

McGill C., Binney J., 1990, MNRAS, 244, 634

Parker J., Lyzenga G., Norton C., Zuffada C., Glasscoe M., Lou J., Donnellan A., 2008, Pure appl. geophys., 165, 497 Portegies Zwart, S.F., Belleman R.G., Geldof P.M., 2007, New Astronomy, 12, 641

Portegies Zwart, S., McMillan S., Groen D., Gualandris A., Sipior M., Vermin W., 2008, New Astronomy, 13, 285

Press, W. H., Teukolsky, S. A., Vetterling, W. T., & Flannery, B. P. 2001, Numerical Recipes in Fortran 77 (Cambridge: Cambridge Univ. Press)

Qian E., 1992, MNRAS, 257, 581

Qian E., 1993, MNRAS, 263, 394

Rahmati A., Jalali M.A., 2009, MNRAS, 393, 1459

Robijn F.H.A., Earn D.J.D., 1996, MNRAS, 282, 1129

Saha P., 1991, MNRAS, 248, 494

Schwarzschild M., 1979, ApJ, 232, 236

Springel V., Hernquist L., 2002, MNRAS, 333, 649

Springel V., 2005, MNRAS, 364, 1105

Sugimoto D., Chikada Y., Makino J., Ito T., Ebisuzaki T., Umemura M., 1990, Nature, 345, 33

Toomre A., 1977, ARA&A, 15, 437

Weinberg M.D., 1999, ApJ, 117, 629

Zang T.A., 1976, Ph.D. Thesis, Massachusetts Institute of Technology

Zhao H., 1996, MNRAS, 278, 488

Zienkiewicz O.C., Taylor R.L., Zhu J.Z., 2005, The Finite Element Method: its basis and fundamentals, 6th edition, Elsevier Butterworth-Heinemann, Oxford